INTERNATIONAL JOURNAL FOR NUMERICAL METHODS IN FLUIDS
Int. J. Numer. Meth. Fluids 2002; **40**:1209–1235 (DOI: 10.1002/fld.417)

A Mach-uniform unstructured staggered grid method

I. Wenneker, A. Segal and P. Wesseling*,†

Department of Applied Mathematical Analysis, Faculty of Information Technology and Systems, Delft University of Technology, Mekelweg 4, 2628 CD, Delft, Netherlands

SUMMARY

A novel Mach-uniform method to compute flows using unstructured staggered grids is discussed. The Mach-uniform method is a generalization of the pressure-correction approach for incompressible flows, and is valid for Mach numbers ranging from 0 (incompressible) to >1 (supersonic). The primary variables ($\rho\mathbf{u}$, p and ρ) are updated sequentially. The grid consists of triangles. A staggered positioning of the variables is employed: the scalar variables are located at the centroids of the triangles, whereas the normal momentum components are positioned at the midpoints of the faces of the triangles. Discretization of the two-dimensional flow equations on unstructured staggered grids is discussed. For the cell face fluxes there is a choice between first-order upwind and central approximation. Flows around the NACA 0012 airfoil with freestream Mach numbers ranging from 0 to 1.2 are computed to demonstrate the Mach-uniform accuracy and efficiency of the proposed method. Copyright © 2002 John Wiley & Sons, Ltd.

KEY WORDS: Mach-uniform methods; unstructured grids; staggered schemes

1. INTRODUCTION

It is well known that the efficiency and accuracy of methods designed to compute compressible flows (Mach number $M>0.2$) deteriorate drastically when M decreases below 0.2. On the other hand, when the Mach number remains uniformly small (below 0.2), an accurate and useful approximation is to consider the flow as incompressible. This observation has led to the development of computing methods exclusively suited for incompressible flows. Neither class of methods is suitable for computing flows in domains in which incompressible subregions as well as compressible subregions occur simultaneously, or for computing weakly compressible flows. For this, methods are required with accuracy and efficiency uniform in the Mach number. We will refer to such unified methods for incompressible and compressible flow computation as Mach-uniform methods.

* Correspondence to: P. Wesseling, Department of Applied Mathematical Analysis, Faculty of Information Technology and Systems, Delft University of Technology, Mekelweg 4, 2628 CD, Delft, The Netherlands.
† E-mail: p.wesseling@its.tudelft.nl

Contract/grant sponsor: The Netherlands Organization for Scientific Research (NWO)

Received December 2000
Revised 24 June 2002

Basically, two strategies can be pursued when designing a Mach-uniform method. The first strategy aims at improving the performance of compressible schemes in the weakly compressible regime. The stiffness problem that occurs when $M \downarrow 0$ can be alleviated by modifying the Euler equations artificially by multiplication of the time derivative by a matrix P^{-1}:

$$P^{-1}\frac{\partial \mathbf{U}}{\partial t} + \nabla \cdot \mathbf{F} = \mathbf{0} \tag{1}$$

where $\mathbf{U}$ is the vector of primitive variables and $\mathbf{F} = \mathbf{F}(\mathbf{U})$ is called the flux function. This procedure is called preconditioning, and the preconditioning matrix $P = P(\mathbf{U})$ should be chosen such that the modified system is less stiff than the original system. The design of P is difficult and remains subject of much research, see References [1–8]. Obviously, time accuracy is lost. Restoring time accuracy is awkward and computationally expensive [8]. Instead of improving accuracy and efficiency of compressible codes, one can take the other way around and incorporate compressibility in incompressible methods. In these methods the pressure serves as a primitive variable. Consequently, Mach-uniform formulations based on incompressible methods are pressure based. Some examples of unified methods following this approach using colocated grids are described in References [9–12], and unified methods on structured staggered grids are introduced in References [13–18]. Essential features in all pressure-based methods are the presence of (i) the pressure or pressure-correction equation, which is a Poisson-like equation yielding the new pressure, and (ii) corrections to the velocity (or momentum) in order to ensure compliance with the continuity equation. A survey of unified methods for compressible and incompressible flows is given in Reference [19, *Chapter* 14].

A common feature of (almost) all established methods for compressible gas dynamics is the use of colocated schemes. For incompressible flows, a straightforward discretization on a colocated grid leads to odd–even oscillations of the pressure. To remedy this, artificial stabilizing measures have to be taken. The most popular method that has evolved is the pressure-weighted interpolation of Reference [20], by which artificial pressure diffusion is introduced in the mass conservation law. This problem of spurious pressure oscillations does not occur with staggered schemes. The difficulty also does not arise in the compressible case. Because on non-orthogonal grids colocated discretization is more straightforward than staggered discretization, colocated schemes are prevalent for fully compressible flows, and have reached a certain degree of maturity. However, staggered schemes can be devised that are accurate on highly non-orthogonal grids, see References [21, 22]. Furthermore, the MAC scheme, i.e. the classic incompressible staggered scheme of [23], can be applied to compressible flows, as shown already in References [14, 15]. For more recent work in this direction, see References [13, 17, 18] and references quoted there. Because an extension of an incompressible scheme is involved, a Mach-uniform method is obtained.

The above remarks pertain to structured schemes. It has become generally recognized that structured grid generation in complicated domains cannot be automated to a satisfactory extent. Therefore, unstructured grids are now receiving widespread attention; for interesting surveys, see References [24, 25]. Most publications on discretization on unstructured grids concern colocated schemes, but staggered schemes would also seem promising, especially for incompressible flows. The staggered incompressible scheme of Reference [23] is generalized to unstructured grids in References [26–32]. The methods presented in these papers require grids of Delaunay–Voronoi type. Staggered incompressible schemes on unstructured grids that

are not generalizations of the scheme of Reference [23] are presented in References [33–36]. In these schemes the full velocity vector is stored at cell faces or cell vertices.

The combination of an unstructured staggered scheme with a Mach-uniform method has apparently not yet been considered; this is the aim of the present paper. Because generation of Delaunay–Voronoi grids is not always easy, see Reference [24], we assume the triangulation to be arbitrary. The paper is organized as follows. In Section 2 the solution procedure, including the Mach-uniform approach, is described. We discuss the finite-volume discretization of the flow equations in Section 3. Numerical results are given in Section 4, and conclusions are gathered in Section 5.

2. SOLUTION PROCEDURE

In Section 2.1 the governing flow equations are briefly described. The difficulties that one encounters with standard compressible schemes when approaching the zero Mach number limit are discussed in Section 2.2. The Mach-uniform solution algorithm is introduced in Section 2.3, and some additional information is given in Section 2.4.

2.1. Governing equations

The Euler equations are given by, using Cartesian tensor notation and the summation convention:

$$\frac{\partial \rho}{\partial t} + (u^\alpha \rho)_{,\alpha} = 0 \tag{2}$$

$$\frac{\partial (\rho E)}{\partial t} + (u^\alpha \rho H)_{,\alpha} = 0 \tag{3}$$

$$\frac{\partial m^\alpha}{\partial t} + (u^\beta m^\alpha)_{,\alpha} = -p_{,\alpha} \tag{4}$$

where $m^\alpha = \rho u^\alpha$ and u^α are the momentum and velocity vectors, ρ is the density, E is the total energy, H is the total enthalpy and p is the pressure. Furthermore, the following thermodynamic relations hold: $H = h + \frac{1}{2}u^2$, $E = e + \frac{1}{2}u^2$, $h = \gamma e$ and $\rho H = \rho E + p$, with h the enthalpy and e the internal energy, and $u^2 = u^\alpha u^\alpha$. The system of equations is closed by the equation of state for a perfect gas:

$$p = \frac{\gamma - 1}{\gamma} \rho h \tag{5}$$

For the specific heat ratio the value $\gamma = \frac{7}{5}$ will be used throughout. The Mach number is defined as $M = u/a$, with u the local flow velocity and $a = \sqrt{(\gamma - 1)h}$ the local speed of sound.

2.2. Difficulties with the zero Mach number limit

In this section, we address some difficulties that may crop up when computing weakly compressible ($M < 0.2$) flows with a standard compressible scheme.

2.2.1. Efficiency or stiffness problem. When using an explicit time-integration scheme, as is often done in standard compressible methods, one needs to satisfy a stability restriction of the following form:

$$\Delta t_c \leqslant C \frac{\Delta x}{u + a} \tag{6}$$

where C is a constant of the order unity, Δx the meshwidth and $(u + a)$ the speed of the acoustic modes. For incompressible flows, the stability restriction is less severe:

$$\Delta t_i \leqslant C \frac{\Delta x}{u} \tag{7}$$

Note that Δt_i, if acoustic effects are absent, is in balance with the physical time scale. We find

$$\frac{\Delta t_c}{\Delta t_i} = \frac{u}{u + a} = \frac{M}{1 + M} \tag{8}$$

so that the numerical time step for compressible methods needs to be much smaller than the physical time step if $M \ll 1$. If no special measures are taken, this results in numerical inefficiency caused by the need to resolve acoustic modes, because (6) remains valid even if there are no acoustic modes. If, instead of time marching to steady state, an iterative steady-state solver is used, a similar convergence problem appears, since for $u \ll (u+a)$ the condition number of the Jacobian $\mathbf{A} = \partial \mathbf{F}/\partial \mathbf{U}$ is given by

$$\kappa = \frac{\lambda_{\max}}{\lambda_{\min}} = \frac{u + a}{u} = 1 + \frac{1}{M} \tag{9}$$

which tends to infinity as M approaches zero, resulting in slow convergence.

2.2.2. Accuracy problem associated with proper choice of units. Another indication of numerical trouble related to the low Mach number limit reveals itself when the momentum equation is made dimensionless. Dimensionless quantities, labelled with tildes, are defined by $\tilde{\mathbf{u}} = \mathbf{u}/u_{\mathrm{r}}$, $\tilde{p} = p/p_{\mathrm{r}}$, and so on, where the quantities indicated by subscripts r are reference values. With a_{r} an estimate for the magnitude of the speed of sound, and $M_{\mathrm{r}} = u_{\mathrm{r}}/a_{\mathrm{r}}$ being representative for the Mach number in the flow, the dimensionless momentum equation becomes (upon deleting tildes for brevity)

$$\frac{\partial m^{\alpha}}{\partial t} + (u^{\beta} m^{\alpha})_{,\beta} = -\frac{1}{\gamma M_{\mathrm{r}}^2} p_{,\alpha} \tag{10}$$

We see that this equation becomes singular as $M_{\mathrm{r}} \downarrow 0$, which spells numerical troubles, e.g. round-off error difficulties, for low subsonic flows with methods developed for compressible flows only.

2.2.3. Accuracy problem related to asymptotic expansion of the continuous and discrete equations. As we saw above, the flow equations become singular as the Mach number tends to zero if these equations are made dimensionless in the way that is customary for

compressible flows. It is interesting to study the way in which solutions of the compressible flow equations converge to solutions satisfying the equations for incompressible flows. To this aim, we postulate an asymptotic expansion of the following form:

$$p(\mathbf{x},t) = p_0(\mathbf{x},t) + \varepsilon p_1(\mathbf{x},t) + \mathcal{O}(\varepsilon^2), \quad \varepsilon = \gamma M_r^2 \tag{11}$$

where we remark that acoustics have been eliminated, and t represents the flow time scale. After introduction of similar expansions for the other dependent variables, the low Mach number limit can be studied, as described for example in References [2, 37, 38], by inserting these expansions in the Euler equations and equating terms with like powers of ε. We get the following results for the continuous flow equations:

- If there is no global expansion or compression, $p_0(\mathbf{x},t) = p_0$ is constant in space and time, where p_0 stands for the constant background pressure level, which can be considered as the global thermodynamic pressure part.
- The expansion leads for terms of the order ε to

$$\frac{\partial m_0^\alpha}{\partial t} + (u_0^\beta m_0^\alpha)_{,\beta} = -(p_1)_{,\alpha}, \quad m_0^\alpha = \rho_0 u_0^\alpha \tag{12}$$

  Since $p_1(\mathbf{x},t)$ ensures compliance with the divergence constraint on the velocity, the term $\varepsilon p_1(\mathbf{x},t)$ is called the incompressible flow part of the pressure.
- In contrast to what is sometimes believed, it is the energy equation (and not the continuity equation) from which the kinematic constraint

$$\nabla \cdot \mathbf{u}_0 = 0 \tag{13}$$

  in the limit of $M_r \downarrow 0$ is derived.

In Reference [2] it is shown that solutions, obtained by means of flux difference schemes, contain pressure fluctuations of the order M_r, while the continuous pressure scales with M_r^2. This loss of accuracy explains why flux difference methods fail to compute weakly compressible flow. As M_r decreases, the solutions do not converge to a reasonable approximation of the incompressible solution.

2.2.4. Weak pressure–density coupling. When computing low subsonic flow, the weak pressure–density coupling has consequences for the choice of primary variables. In incompressible flows, the density is constant along particle lines, but the pressure is not. Therefore, for low Mach number flow it is not a good idea to use density as a primary variable and compute the pressure from the equation of state. In that case we would, in the limit $M_r \downarrow 0$, compute the zeroth-order pressure p_0 in (11) which is not the pressure component we need. The other way around, i.e. computation of the pressure and afterwards evaluation of the density through the equation of state or the continuity equation, does not degrade performance for decreasing Mach numbers, and can without problem even be applied for incompressible flows. But standard compressible methods are density based, and consequently suffer from weak pressure–density coupling when the Mach number is small.

2.3. Mach-uniform solution algorithm

We discuss in this section the pressure-based conservative Mach-uniform solution algorithm recently introduced in Reference [18]. With this Mach-uniform scheme one can compute flow with a Mach number ranging from the incompressible limit $M_r = 0$ up to supersonic flow $M_r > 1$, with nearly uniform efficiency and accuracy. This uniformity in the Mach number will be demonstrated in Section 4. In the incompressible limit, the Mach-uniform scheme reduces to the standard (incompressible) pressure-correction scheme.

2.3.1. Dimensionless formulation. The pressure is non-dimensionalized as follows:

$$\tilde{p} = \frac{p - p_r}{\rho_r u_r^2} \tag{14}$$

with p_r a suitable reference value, to be defined later. This particular definition of the dimensionless pressure is an essential feature of the present Mach-uniform formulation. The same pressure scaling is also used in References [13, 17, 18]. The physical significance of (14) can be found when we return to (11). This shows that with the obvious alternative $\tilde{p}_s = p/p_0$ the variation of $\tilde{p}_s$ is $\mathcal{O}(M_r^2)$, so there is a risk of loss of significant digits for M_r small. Note that $\tilde{p}_s$ is the dimensionless pressure as commonly defined in compressible schemes. However, substitution of (11) in (14) gives (choosing $p_r = p_0$)

$$\tilde{p} = \frac{p_1}{p_r} + \mathcal{O}(M_r^2) \tag{15}$$

This shows that $\tilde{p}$ has the nice property of being $\mathcal{O}(1)$ as $M_r \downarrow 0$. Of course, this is already obvious from (14), if one thinks of Bernoulli's theorem. Furthermore, with (11) the singular factor $1/\gamma M_r^2$ disappears from the momentum equation. Non-dimensionalization as described above leaves the continuity and momentum equation invariant. The dimensionless equation of state yielding the enthalpy is given by, omitting from now on the tildes:

$$h = \frac{1}{\rho}(1 + \gamma M_r^2 p) \tag{16}$$

When written in the form

$$\rho = \frac{1}{h}(1 + \gamma M_r^2 p) \tag{17}$$

it is immediately clear that, as it should, the density becomes independent of the pressure in the limit $M_r \downarrow 0$. The dimensionless energy equation (3) can be written in the following form:

$$M_r^2 \left\{ \frac{\partial}{\partial t}\left[p + \frac{1}{2}(\gamma - 1)\rho u^\gamma u^\gamma \right] + \left[u^\alpha \left(\gamma p + \frac{1}{2}(\gamma - 1)\rho u^\gamma u^\gamma \right) \right]_{,\alpha} \right\} + u^\gamma_{,\gamma} = 0 \tag{18}$$

Remark that, as already stated in Section 2.2, it is the energy equation from which the kinematic constraint $(\nabla \cdot \mathbf{u}) = 0$ is derived in the limit $M_r \downarrow 0$. Equation (18) forms the basis for the Mach-uniform pressure-correction equation, to be discussed below. Inclusion of the diffusive terms in (18) can be done without problem, but will not be discussed in this paper.

2.3.2. Mach-uniform pressure-correction equation. The following relation between the momentum at time-level $n+1$ and the predictor of the momentum is postulated:

$$\mathbf{m}^{n+1} = \mathbf{m}^* - \Delta t \nabla \delta p \tag{19}$$

where $\Delta t = t^{n+1} - t^n$ is the time step and the pressure correction is defined as

$$\delta p = p^{n+1} - p^n \tag{20}$$

Inserting

$$\mathbf{m}^* = \rho^{n+1}\mathbf{u}^* \tag{21}$$

where $\mathbf{u}^*$ is the predictor of the velocity, and

$$(\rho \mathbf{u}^2)^{n+1} = (\mathbf{m}^2/\rho)^{n+1} = (\mathbf{m}^* - \Delta t \nabla \delta p)^2/\rho^{n+1} \tag{22}$$

into (18) and discretizing in time with Euler implicit yields a non-linear equation for δp:

$$\begin{aligned} & M_r^2 \left\{ \frac{\delta p}{\Delta t} + \frac{1}{2}(\gamma - 1) \frac{(\mathbf{m}^* - \Delta t \nabla \delta p)^2/\rho^{n+1} - (\mathbf{m}^n)^2/\rho^n}{\Delta t} \right. \\ & \left. + \nabla \cdot \left[\left(\mathbf{u}^* - \frac{\Delta t}{\rho^{n+1}} \nabla \delta p \right) \left(\gamma (p^n + \delta p) + \frac{1}{2}(\gamma - 1)(\mathbf{m}^* - \Delta t \nabla \delta p)^2/\rho^{n+1} \right) \right] \right\} \\ & + \nabla \cdot \left(\mathbf{u}^* - \frac{\Delta t}{\rho^{n+1}} \nabla \delta p \right) = 0 \end{aligned} \tag{23}$$

For brevity, we have written $\mathbf{m}^2 = \mathbf{m} \cdot \mathbf{m}$. After a suitable linearization and some rearranging we arrive at the following Mach-uniform pressure-correction equation:

$$\begin{aligned} & M_r^2 \left\{ \frac{\delta p}{\Delta t} + \frac{1}{2}(\gamma - 1) \frac{[(\mathbf{m}^*)^2 - 2\Delta t \mathbf{m}^* \cdot \nabla \delta p]/\rho^{n+1} - (\mathbf{m}^n)^2/\rho^n}{\Delta t} \right\} \\ & + \nabla \cdot \left[\mathbf{u}^* \left(1 + \gamma M_r^2 (p^n + \delta p) + \frac{1}{2}(\gamma - 1) M_r^2 (\mathbf{m}^*)^2/\rho^{n+1} \right) \right] \\ & - \Delta t \nabla \cdot \left\{ \left[\left(1 + \gamma M_r^2 p^n + \frac{1}{2}(\gamma - 1) M_r^2 (\mathbf{m}^*)^2/\rho^{n+1} \right) \Big/ \rho^{n+1} \right] \nabla \delta p \right\} = 0 \end{aligned} \tag{24}$$

For $M_r \downarrow 0$, the pressure-correction equation for incompressible flows is recovered. Furthermore, one can prove that $H = \text{constant}$ is, as it should, a steady solution of (24).

2.3.3. Mach-uniform sequential update procedure. Definition of 'left' and 'right' state vectors (containing all primitive variables) at a control volume face is the starting point for the familiar flux difference and flux splitting schemes for the Euler equations. In iterative solution methods, the elements of the state vector in a cell are usually updated collectively. But definition and collective updates of such state vectors are not naturally given on a staggered grid; this will

be the topic of Section 3. On the other hand, discretization by a simple finite difference or finite-volume scheme for each primary variable separately is natural on a staggered grid. It is also natural to update the primary variables sequentially in a time stepping or iterative procedure. For this purpose, the implicit Euler method is used. For the primary variables we take $\mathbf{m}$, ρ and p. The following Mach-uniform solution algorithm is proposed:

1. Compute ρ^{n+1}, the solution vector of the density at time-level $n+1$, from

$$R_\rho \frac{\rho^{n+1}-\rho^n}{\Delta t} + D(\mathbf{u}^n \rho^{n+1}) = 0 \tag{25}$$

   Here R_ρ is a diagonal matrix containing the area of the control volumes, D corresponds to the discrete divergence operator, and $\mathbf{u}^n$ is the solution vector of the velocity at time-level n.
2. Compute the momentum prediction $\mathbf{m}^*$ from

$$R_m \frac{\mathbf{m}^*-\mathbf{m}^n}{\Delta t} + C(\mathbf{u}^n)\mathbf{m}^* = -R_m G p^n \tag{26}$$

   where R_m refers to a diagonal matrix containing the area of the control volumes, C is the discrete convection operator, G the discrete gradient operator and p the solution vector of the pressure at time-level n.
3. The new pressure follows from the pressure-correction equation (24).
4. A correction, see (19), is added to the predictor of the momentum to obtain the momentum $\mathbf{m}^{n+1}$.
5. The new enthalpy follows from (16).

For (nearly) incompressible flows, the density variations should remain (nearly) zero, which is ensured by inserting the (nearly) divergence-free $\mathbf{u}^n$ in (25). When applied to incompressible flows with constant density, steps 1 and 5 in the Mach-uniform solution algorithm are not of interest, and the standard pressure-correction approach for incompressible flows is recovered.

2.4. Additional information

The linear systems are solved by means of ILU-preconditioned GMRES (steps 1 and 2 of the above algorithm) and ILU-preconditioned Bi-CGSTAB (step 3). With $\mathbf{w}^n = (w_1^n, w_2^n, \ldots)$ the solution vector of quantity w at time-level n, a stationary problem is said to have converged sufficiently to steady state if the termination criterion

$$\|\mathbf{w}^{n+1}-\mathbf{w}^n\|_2 \leqslant \varepsilon \frac{1-\lambda}{\lambda} \|\mathbf{w}^{n+1}\|_2 \tag{27}$$

with a user-specified relative accuracy ε, is satisfied for all primary variables. The rate of convergence in (27) is defined by

$$\lambda = \frac{\|\mathbf{w}^{n+1}-\mathbf{w}^n\|_2}{\|\mathbf{w}^n-\mathbf{w}^{n-1}\|_2} \tag{28}$$

and $\|\cdot\|_2$ is the standard L_2-norm. This stopping criterion is based on the assumption of linear convergence behaviour.

3. FINITE-VOLUME DISCRETIZATION

In this section, spatial discretization of the flow equations on unstructured staggered grids is discussed. The staggered positioning of the variables on triangular grids is introduced in Section 3.1. As stated before, it is not possible to define state vectors containing all primitive variables. This is why schemes based on Riemann solvers cannot be applied. On the other hand, a segregated approach is natural on a staggered grid. A finite-volume scheme is used for each primary variable, for which we take $\mathbf{m}$, ρ and p. It can be shown, see Reference [39] for a thorough discussion, that our scheme conserves mass, momentum and energy, and this suggests, through the Lax–Wendroff theorem, that the Rankine–Hugoniot conditions are satisfied. As seen below, the numerical fluxes follow from simple upwind or central approximations, and require in principle less computing than the numerical fluxes commonly encountered in colocated schemes. Discretization of the momentum, continuity and Mach-uniform pressure-correction equation forms the topics in Sections 3.2, 3.3 and 3.4, respectively.

3.1. Staggered grid arrangement

We will restrict ourselves to two dimensions, and consider grids consisting of triangles solely. In Figure 1 the employed staggered placement of variables in the grid is shown. At the cell centroids the scalar variables (e.g. p, ρ and h) are located. At every face e there are two unit normal vectors $\mathbf{n}_e$, pointing in opposite directions. By some unambiguous procedure we select at each face one of these to be the so-called unique normal vector $\mathbf{N}_e$. The normal momentum components $m = \mathbf{m} \cdot \mathbf{N}$ are stored at the midpoints of the faces. This placement of the variables is similar to the classic staggered scheme on structured grids with quadrilateral cells as introduced by Harlow and Welch [14, 15, 23] and which is used by our group for compressible flows in References [13, 17, 18, 39].

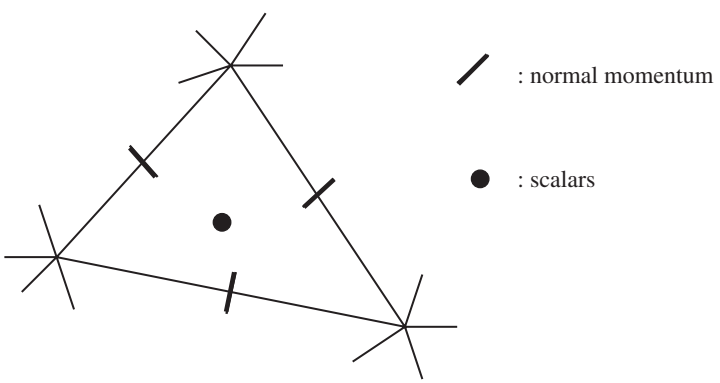

Figure 1. Staggered positioning of the variables in an unstructured grid.

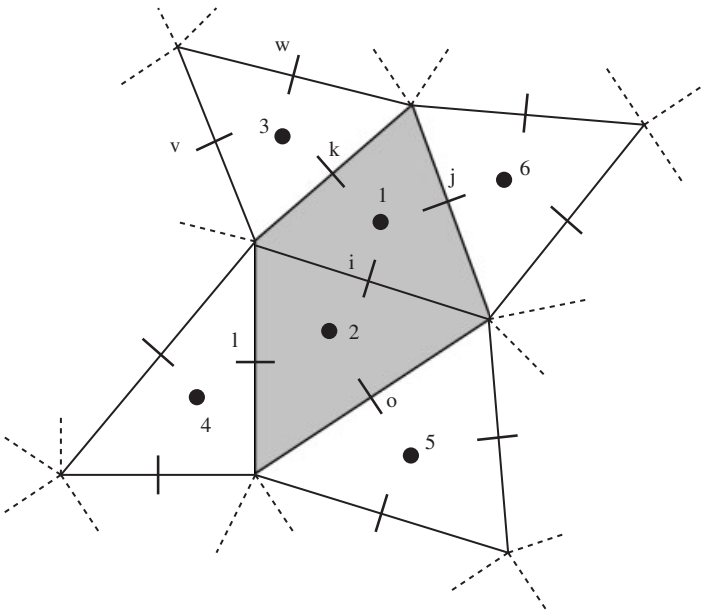

Figure 2. The CV for the normal momentum component at face i is shaded. Numbers denote cells, while faces are indicated by letters.

3.2. *Discretization of the momentum equation*

The first step in deriving a discrete equation for $m_i = \mathbf{m}_i \cdot \mathbf{N}_i$ is to project the momentum equation (4) on $\mathbf{N}_i$:

$$\frac{\partial m_i}{\partial t} + \nabla \cdot [\mathbf{u}(\mathbf{m} \cdot \mathbf{N}_i)] = -\nabla p \cdot \mathbf{N}_i \tag{29}$$

The flux consists of a convective and pressure part, that are approximated separately. This is also done for instance in the AUSM scheme [40], and in Jameson's CUSP scheme [41, 42]. We integrate (29) over a suitably chosen control volume (CV). For the choice of the CV there are various possibilities, see for example [26–31] for the choice made in the covolume method or [32] for the choice made by Perot. We choose the union of the two triangles adjacent to face i, see Figure 2, as CV for m_i. For a boundary face at which the normal momentum is not given, the CV consists of the corresponding boundary cell.

3.2.1. Time derivative. Integration of the time derivative over the CV in (29) is done in the usual manner:

$$\frac{\mathrm{d}}{\mathrm{d}t} \int_{\mathrm{CV}} m_i \, \mathrm{d}\mathbf{x} \approx \Omega_i \, \frac{m_i^{n+1} - m_i^n}{\Delta t}$$

where Ω_i is the area of the CV, Δt the time step and the superscript refers to the time level.

3.2.2. Convection term. Integration of the convection term over the CV of Figure 2 results in

$$\int_{\mathrm{CV}} \nabla \cdot [\mathbf{u}(\mathbf{m} \cdot \mathbf{N}_i)]\, \mathrm{d}\mathbf{x} = \oint_{\partial \mathrm{CV}} (\mathbf{u} \cdot \mathbf{n})(\mathbf{m} \cdot \mathbf{N}_i)\, \mathrm{d}\Gamma \approx \sum_{e(i)} (\mathbf{u}_e \cdot \mathbf{N}_e)(\mathbf{m}_e \cdot \mathbf{N}_i)\bar{l}_e \tag{30}$$

where $\mathbf{n}$ is the outward unit normal with respect to the CV. In the last step we defined

$$\bar{l}_e = l_e(\mathbf{n}_e \cdot \mathbf{N}_e) \tag{31}$$

where we note that $(\mathbf{n}_e \cdot \mathbf{N}_e) = \pm 1$. The summation is over the faces of the CV, i.e. over the faces in $e(i) \in \{k, l, o, j\}$. The implicit Euler scheme and Picard linearization are used, which means that $\mathbf{u}_e$ is evaluated at time-level n and $\mathbf{m}_e$ at time-level $n+1$; for brevity, time-level superscripts are omitted. We further specify computation of the contribution to the convection term of face k, i.e. the term $(\mathbf{u}_k \cdot \mathbf{N}_k)(\mathbf{m}_k \cdot \mathbf{N}_i)\bar{l}_k$.

Approximation of the convecting normal velocity $(\mathbf{u}_k \cdot \mathbf{N}_k)$: At face k, the normal velocity $u_k = \mathbf{u}_k \cdot \mathbf{N}_k$ follows from

$$u_k = \frac{m_k}{\rho_{k,\mathrm{av}}}, \qquad \rho_{k,\mathrm{av}} = \frac{\Omega_3}{\Omega_1 + \Omega_3}\,\rho_1 + \frac{\Omega_1}{\Omega_1 + \Omega_3}\,\rho_3 \tag{32}$$

Here m_k is the given normal momentum component and $\rho_{k,\mathrm{av}}$ approximates the density at face k by means of a weighted averaging, with Ω_1 and Ω_3 referring to the areas of the adjacent cells, see Figure 2. Note that if the density is constant, as is often the case for incompressible flows, then (32) is exact.

Approximation of the convected momentum $(\mathbf{m}_k \cdot \mathbf{N}_i)$: Assume that the fluid moves from cell 3 to 1. We use the normal momentum components m_v and m_w in cell 3 to approximate $\mathbf{m}_k \cdot \mathbf{N}_i$. Since faces v and w are in the same triangle, the normal vectors $\mathbf{N}_v$ and $\mathbf{N}_w$ are never parallel. As a consequence, there exists a unique solution to the reconstruction coefficients η_v and η_w, defined in

$$\mathbf{N}_i = \eta_v \mathbf{N}_v + \eta_w \mathbf{N}_w \tag{33}$$

Substitution gives

$$\begin{aligned} \mathbf{m}_k \cdot \mathbf{N}_i &= \mathbf{m}_k \cdot (\eta_v \mathbf{N}_v + \eta_w \mathbf{N}_w) \approx \eta_v (\mathbf{m}_v \cdot \mathbf{N}_v) + \eta_w (\mathbf{m}_w \cdot \mathbf{N}_w) \\ &= \eta_v m_v + \eta_w m_w \end{aligned}$$

with equality for constant momentum vector fields. If the fluid moves from cell 1 to 3, $\mathbf{m}_k$ is approximated in terms of m_i and m_j. In the same way as before we arrive at

$$\mathbf{m}_k \cdot \mathbf{N}_i \approx m_i$$

Summarizing, the first-order upwind approximation for $(\mathbf{m}_k \cdot \mathbf{N}_i)$ is

$$\mathbf{m}_k \cdot \mathbf{N}_i = \begin{cases} \eta_v m_v + \eta_w m_w & \text{if } u_k \bar{l}_k < 0 \\ m_i & \text{if } u_k \bar{l}_k > 0 \end{cases} \tag{34}$$

The following central scheme is found to give good results in the absence of steep gradients:

$$\mathbf{m}_k \cdot \mathbf{N}_i = \frac{1}{2}(m_i + \eta_v m_v + \eta_w m_w) \tag{35}$$

In the numerical examples described in this paper, only the first-order upwind scheme is employed.

3.2.3. Pressure gradient. The projected pressure gradient is numerically integrated as follows:

$$\int_{\mathrm{CV}} \nabla p \cdot \mathbf{N}_i \, \mathrm{d}\mathbf{x} = \Omega_i (\nabla p \cdot \mathbf{N})_i \tag{36}$$

For the evaluation of $(\nabla p \cdot \mathbf{N})_i$, the path-integral formulation as introduced for structured grids in Reference [43] is used. First an approximation of the pressure gradient $(\nabla p)_i$ at face i is made, after which the inner product with $\mathbf{N}_i$ is taken. This will result in a centred pressure approximation, which, as we will see in the numerical experiments, rules out spurious modes. We start with the identity

$$p_b - p_a = \int_a^b \nabla p \cdot \mathrm{d}\mathbf{x}$$

where a and b refer to points with co-ordinates $\mathbf{x}_a$ and $\mathbf{x}_b$. This expression is approximated by

$$p_b - p_a \approx (\nabla p)_{ab} \cdot (\mathbf{x}_b - \mathbf{x}_a) \tag{37}$$

where $\mathbf{x}_{ab}$ is a point in the vicinity of $\mathbf{x}_a$ and $\mathbf{x}_b$, and $p_a = p(\mathbf{x}_a)$ and $p_b = p(\mathbf{x}_b)$. Application of (37) to a path from cell-centre 1 to 2, see Figure 2, gives

$$p_2 - p_1 \approx (\nabla p)_i \cdot (\mathbf{x}_2 - \mathbf{x}_1) \tag{38}$$

To determine $(\nabla p)_i$ one additional relation is required. The use of (37) for a path from 5 to 3 leads to

$$p_3 - p_5 \approx (\nabla p)_i \cdot (\mathbf{x}_3 - \mathbf{x}_5)$$

and, similarly,

$$p_4 - p_6 \approx (\nabla p)_i \cdot (\mathbf{x}_4 - \mathbf{x}_6)$$

We use the average of these expressions:

$$p_3 - p_6 + p_4 - p_5 \approx \nabla p_i \cdot (\mathbf{x}_3 - \mathbf{x}_6 + \mathbf{x}_4 - \mathbf{x}_5) \tag{39}$$

Equations (38) and (39) determine $(\nabla p)_i$. The stencil for the pressure gradient consists of the six centroids depicted in Figure 2. Since for a linear pressure field we have equality in (37), the approximation is exact for linear pressure fields. Solution of system (38)–(39) leads to

$$(\nabla p \cdot \mathbf{N})_i = \sum_{j=1}^{6} \gamma_j p_j \tag{40}$$

With $\mathbf{x}_j = (x_j, y_j)$, $\mathbf{N}_i = (N_x, N_y)$ and defining the auxiliary coefficients

$$a_{11} = x_2 - x_1, \quad a_{12} = y_2 - y_1$$

$$a_{21} = x_3 - x_6 + x_4 - x_5, \quad a_{22} = y_3 - y_6 + y_4 - y_5$$

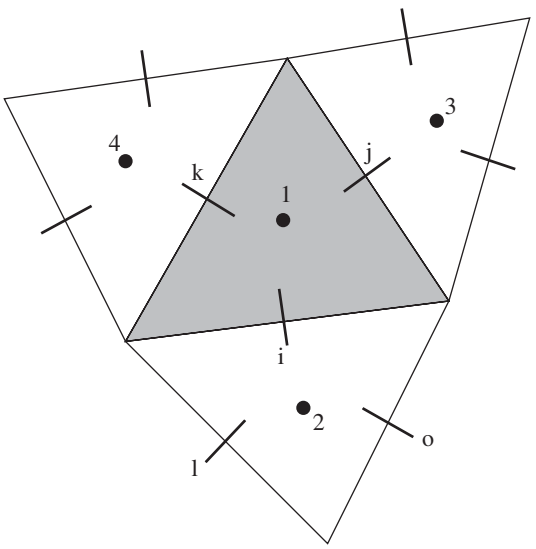

Figure 3. The CV for the continuity and Mach-uniform pressure-correction equation is shaded.

the gradient coefficients γ_j are given by

$$\gamma_1 = -\gamma_2 = \frac{a_{21}N_y - a_{22}N_x}{a_{11}a_{22} - a_{12}a_{21}}$$

$$\gamma_3 = \gamma_4 = -\gamma_5 = -\gamma_6 = \frac{a_{11}N_y - a_{12}N_x}{a_{11}a_{22} - a_{12}a_{21}}$$

A special situation occurs when vector $(\mathbf{x}_2 - \mathbf{x}_1)$ is parallel to $\mathbf{N}_i$. The path-integral method then reduces to the well-known finite difference approximation:

$$(\nabla p \cdot \mathbf{N})_i = \frac{p_2 - p_1}{|\mathbf{x}_2 - \mathbf{x}_1|}$$

When one or more centroids in the stencil are absent, which occurs in the vicinity of a boundary, the paths in (39) are truncated such as to use only existing centroids.

3.3. Discretization of the continuity equation

The triangles serve as CV for the scalar (continuity and Mach-uniform pressure correction) equations. Integration of (2) over triangle T_1, see Figure 3, is done as follows:

$$\int_{T_1} \frac{\partial \rho}{\partial t}\,\mathrm{d}\mathbf{x} + \int_{T_1} \nabla \cdot (\mathbf{u}\rho)\,\mathrm{d}\mathbf{x} = \frac{\mathrm{d}}{\mathrm{d}t}\int_{T_1} \rho\,\mathrm{d}\mathbf{x} + \oint_{\partial T_1} (\rho\mathbf{u}\cdot\mathbf{n})\,\mathrm{d}\Gamma$$

$$\approx \Omega_1 \frac{\rho_1^{n+1} - \rho_1^n}{\Delta t} + \sum_{e(1)} u_e \rho_e \bar{l}_e = 0 \tag{41}$$

with $\mathbf{n}$ the outward unit normal at the boundary ∂T_1 of the control volume. The area of T_1 is denoted by Ω_1, summation takes place over the three faces in $e(1) \in \{i,j,k\}$ of cell 1, and $\bar{l}_e$ is defined in (31). Note that we do not insert $m_e = \rho_e u_e$, with m_e already evaluated from the momentum equation. The reason is that we use an upwind bias in order to introduce a measure of irreversibility, which is beneficial for satisfying the entropy condition, see also [11, 13, 44]. The velocity component u_e is evaluated using $u_e = m_e^n / \rho_{e,\mathrm{av}}^n$, see (32). The first order upwind approximation for ρ_i is

$$\rho_i = \begin{cases} \rho_1 & \text{if } u_i \bar{l}_i > 0 \\ \rho_2 & \text{if } u_i \bar{l}_i < 0 \end{cases} \tag{42}$$

In the absence of steep gradients, the central scheme (not employed in the computations described in this paper):

$$\rho_i = \frac{1}{2}(\rho_1 + \rho_2) \tag{43}$$

is found to give good results. Since an implicit Euler time-integration scheme is adopted, the density in the convection term is taken at the new time level.

3.4. Discretization of the Mach-uniform pressure-correction equation

The Mach-uniform pressure-correction equation (24) is integrated over each triangle. The convection term (in the second line) is evaluated in a similar way as the convection term in the continuity equation. In the last line, the expression between square parentheses [ ] in the Laplacian term is obtained by means of weighted averaging similar to (32). The only aspect concerning discretization of (24) that we have not addressed yet, is the evaluation of the terms $\mathbf{m}^2$ and $\mathbf{m} \cdot \nabla \delta p$ in the cell centre. This problem comes down to evaluation of a vector $\mathbf{v}_1 = (v_{x,1}, v_{y,1})$ in the cell centre using the given normal components $v_e = \mathbf{v}_e \cdot \mathbf{N}_e$ at the three cell faces of cell 1. Since we have three knowns and two unknowns, the use of a least-squares approach appears as an obvious choice. If the flow field is smooth, we have $v_e = \mathbf{v}_e \cdot \mathbf{N}_e \approx (\mathbf{v}_1 \cdot \mathbf{N}_e)$ for all $e(1) \in \{i,j,k\}$. We choose $\mathbf{v}_1$ such that the least-squares functional

$$\mathscr{F}(\mathbf{v}_1) = \sum_{e(1)} [v_e - (\mathbf{v}_1 \cdot \mathbf{N}_e)]^2 \tag{44}$$

is minimal. The minimum of this functional is found there where

$$\frac{\partial \mathscr{F}}{\partial v_{x,1}} = \sum_{e(1)} -2N_{x,e}(v_e - v_{x,1}N_{x,e} - v_{y,1}N_{y,e}) = 0$$

$$\frac{\partial \mathscr{F}}{\partial m_{y,1}} = \sum_{e(1)} -2N_{y,e}(v_e - v_{x,1}N_{x,e} - v_{y,1}N_{y,e}) = 0$$

This boils down to solving the system

$$\begin{bmatrix} \sum N_{x,e}^2 & \sum N_{x,e}N_{y,e} \\ \sum N_{x,e}N_{y,e} & \sum N_{y,e}^2 \end{bmatrix} \begin{bmatrix} v_{x,1} \\ v_{y,1} \end{bmatrix} = \begin{bmatrix} \sum v_e N_{x,e} \\ \sum v_e N_{y,e} \end{bmatrix}$$

with summation again over the three cell faces. This method is discussed in Reference [45] for grids consisting of quadrilaterals.

4. NUMERICAL RESULTS

The difficult issue of convergence to physically relevant weak solutions of the Euler equations, which requires satisfaction of the Rankine–Hugoniot jump conditions and the entropy condition (which rules out expansion shocks), for the unstructured staggered grid scheme is addressed in Reference [39]. In that paper we demonstrated, by computing solutions on arbitrary two-dimensional (2D) unstructured grids to Riemann problems, that our scheme converges to the entropy solution. Note that only for the Osher scheme [46] these solutions do not contain spurious modes, and their accuracy is similar to that of the well-established Roe and AUSM schemes. A matter that we have not addressed in Reference [39] concerns the accuracy of the spatial discretization. In Section 4.1, we demonstrate by means of a grid refinement study that the present unstructured staggered scheme has, as was to be expected, first-order spatial accuracy. Four distinct types of flow (low subsonic, subcritical, transonic and supersonic) around an NACA 0012 airfoil are studied in Section 4.2 in order to demonstrate Mach-uniform accuracy and efficiency of the present scheme.

4.1. Flow in a channel with bump: grid refinement study

Subsonic flow in a channel with a 10% sinusoidal arc bump was chosen to show that the spatial accuracy of our unstructured scheme is first order, and that the accuracy is relatively insensitive to the shape of the triangles. The curve describing the lower wall of the domain is chosen such that it is differentiable. A grid refinement study on what we call rectangular and general grids, to be referred to as r and g, respectively, has been performed. The boundaries of the channel, having length 3 and height 1, are divided into $3n \times n$ nodal points, with n an integer. In Figure 4 the unstructured grids with $n = 8$ are shown. Freestream flow is taken as initial condition. The stationary solution is computed, using a relative accuracy (see Equation (27)) equal to 10^{-2}, on grids with n varying from 8 to 160. The Mach number isolines of the converged solutions obtained with the first-order upwind scheme on grids with $n = 32$ are depicted in Figure 5. Note that the solutions on both unstructured grids are virtually the same. For $n \to \infty$, the solutions become indistinguishable. The Mach number and entropy at the lower boundary are shown, for grids of type g, in Figure 6. For inviscid and subsonic flow the solution should be symmetric with respect to the symmetry axis of the problem. The asymmetry, visible in Figures 5 and 6, is due to the numerical diffusion introduced by the first-order upwind scheme. This asymmetry becomes, as one observes, less with finer grids.

In inviscid subsonic flows, the entropy $S = \ln(p/\rho^{\gamma})$ is a constant, so that variations in the computed entropy can be regarded as a measure for the numerical error. This naturally leads to the following way to quantify the error of the numerical scheme:

$$E_h = \int_{\Gamma} |S_h| \, \mathrm{d}\Gamma \tag{45}$$

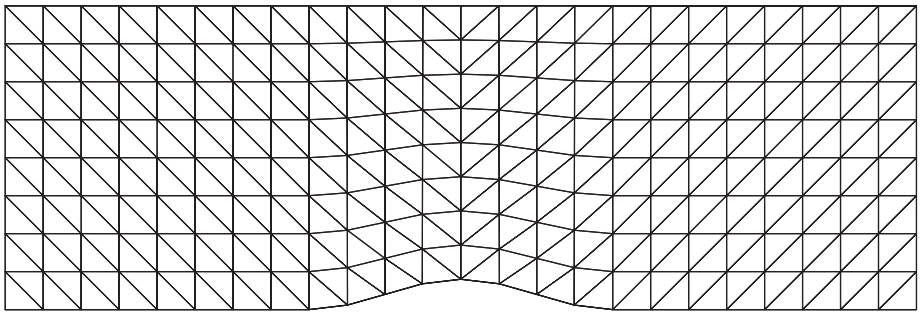

(a)

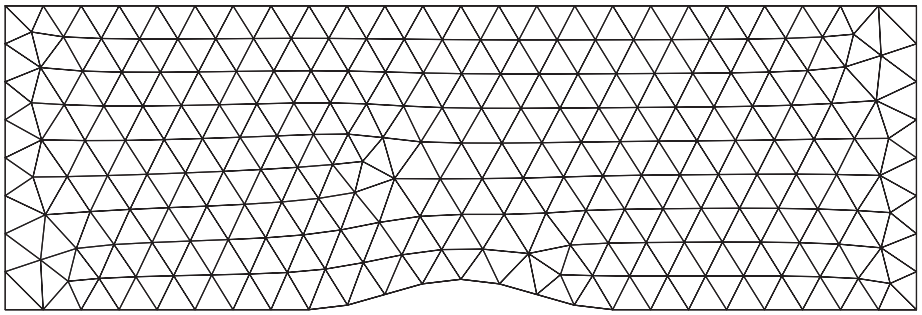

(b)

Figure 4. Example of grids of type r (a) and g (b), with $n = 8$, for subsonic flow over a sinusoidal bump.

where S_h is the computed entropy along the lower boundary Γ at a grid with meshwidth h; we choose $h = 1/n$. When h is small, the error is expected to behave as

$$E_h = Kh^p \tag{46}$$

where p is the order of the numerical method, and K is a constant. Plotting $\ln(E_h)$ versus $\ln(h)$ gives, see Figure 7, for h small a slope roughly equal to $p = 1$. Hence, the first-order upwind scheme is, as was to be expected, first-order accurate in space.

4.2. Flows around the NACA 0012 airfoil

Flows around airfoils provide excellent test cases for CFD codes, since these flows contain much of the physics involved in aerodynamics while the problem definition, including the geometry, is relatively easy. Four different kinds of inviscid flows, characterized by the freestream Mach number M_∞ and angle of incidence α, around the NACA 0012 airfoil have been considered: (i) low subsonic flow with $M_\infty = 0, 10^{-3}, 10^{-2}, 10^{-1}$ and $\alpha = 0°$; (ii) subcritical flow with $M_\infty = 0.63$ and $\alpha = 2°$; (iii) transonic flow with $M_\infty = 0.8$ and $\alpha = 1.25°$, and (iv) supersonic flow with $M_\infty = 1.2$ and $\alpha = 0°$. The accuracy of the results is discussed in Section 4.2.1. The efficiency of the Mach-uniform (MU) approach forms the subject of

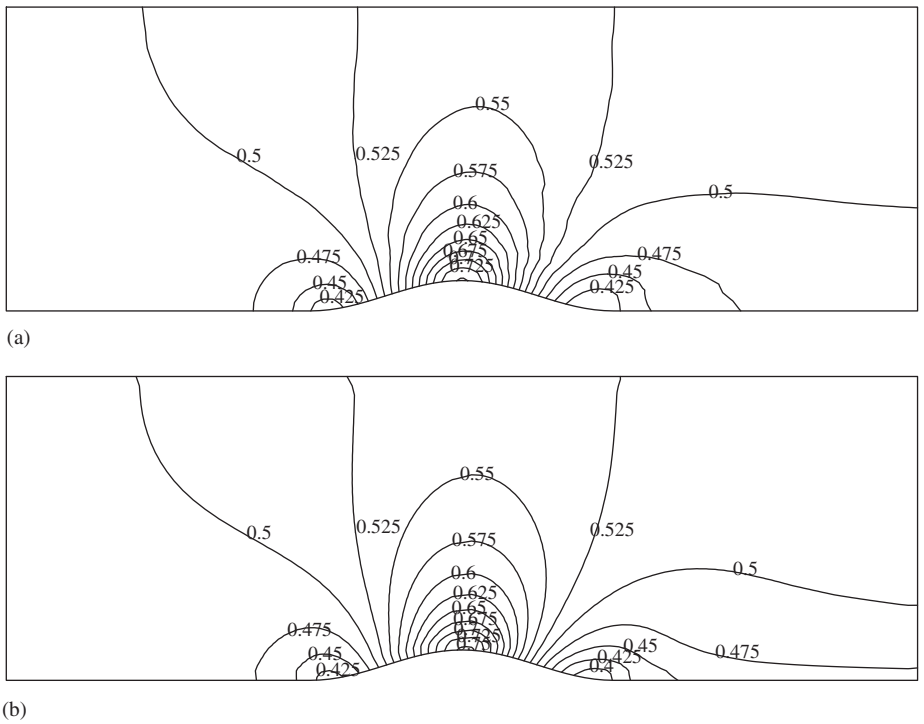

Figure 5. The Mach isolines of subsonic flow over a bump, computed on grids of type g (a) and r (b), with $n = 32$.

Section 4.2.2. For future reference, we define the Courant–Friedrichs–Lewy (CFL) number as follows:

$$\sigma = \max \frac{(u + a)\Delta t}{\Delta x}, \quad \Delta x = \min_i \left(\Omega_i \Big/ \max_{e(i)} l_e \right) \tag{47}$$

where a is the local speed of sound and u the local flow velocity. The minimal meshwidth Δx is the minimum of the ratio of the area of the triangle and the length of the corresponding triangle's faces. Unless stated otherwise, the grid partly depicted in Figure 8 is used. With the leading and trailing edge of the airfoil located at co-ordinates $(0, 0)$ and $(1, 0)$, the left lower and right upper co-ordinates of the rectangle defining the considered flow domain are given by $(-3, -5)$ and $(5, 5)$. Hence, the outer boundary is too close to the airfoil, especially for transonic flow, for accurate results. This grid contains 9610 cells, 14 612 faces and 5002 vertices, of which 320 are positioned at the airfoil, and the minimal meshwidth equals 1.0×10^{-3}.

4.2.1. Accuracy aspects. Low subsonic flow: As discussed in Section 2.2, the accuracy and efficiency of standard compressible flow solvers deteriorate with decreasing Mach number. For standard solvers, sometimes the $M_r = 0.1$ solution of the flow around an airfoil is even

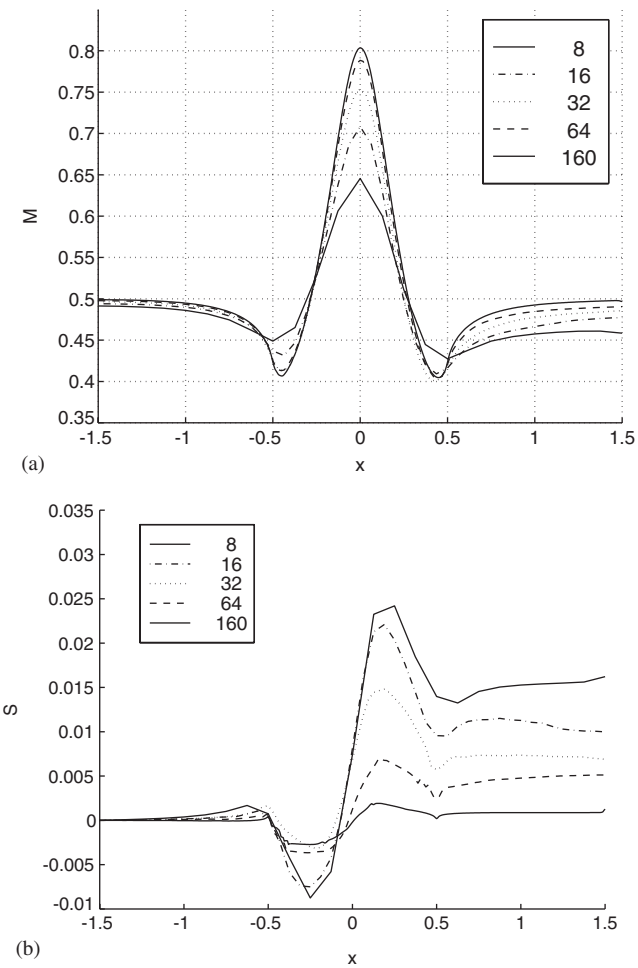

Figure 6. The Mach number (a) and the entropy (b) at the lower wall for various values of n at grids of type g.

closer to the incompressible one than is the $M_r = 10^{-3}$ solution, see References [2, 47]. Therefore, flows parameterized by $M_r = 0,\ 10^{-3},\ 10^{-2},\ 10^{-1}$ form a good test case to study the low Mach number behaviour of compressible schemes. The angle of attack is 0°. We chose $\varepsilon = 10^{-2}$ for the relative stationary accuracy, see Equation (27). The MU algorithm reduces to the incompressible pressure-correction algorithm when $M_r = 0$ is inserted, and this is confirmed experimentally. The isobars of the incompressible solution are shown in Figure 9a. The pressure fluctuations, non-dimensionalized as in Equation (14), should remain constant for M_r small, see also expression (15). We observe in Figure 9 that this is indeed the case: the computed isobars for $M_r = 0,\ 10^{-3}$ and 10^{-2} are virtually identical, and in the $M_r = 0.1$ result compressibility effects start to play a non-negligible role. Hence, the MU approach clearly does not suffer from loss of accuracy in the low Mach number regime.

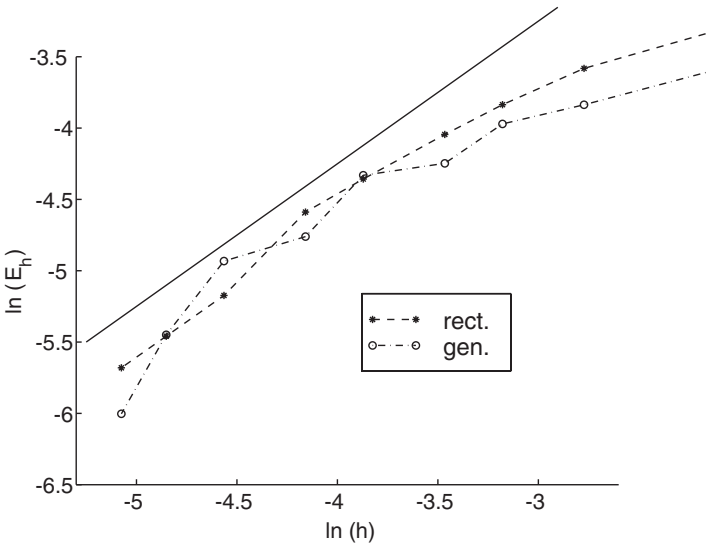

Figure 7. The natural logarithm of the error E_h versus the meshwidth h, for the two types of grids considered. The continuous line is an auxiliary line with slope 1.

Subcritical flow around the NACA 0012 airfoil: Subcritical flow around the NACA 0012 airfoil with a freestream Mach number of $M_\infty = 0.63$ and an angle of attack $\alpha = 2°$ is computed using a relative accuracy of 10^{-2}. The computed isobars and Mach number at the airfoil are illustrated in Figure 10. The computed values for the lift coefficient, drag coefficient and maximum Mach number in the domain are, respectively, 0.27, 1.1×10^{-2} and 0.875, whereas the benchmark solution [48] yields 0.33, 0 and 0.99 for these quantities. The differences are attributed to the fact that we use a first-order upwind scheme and a relatively coarse grid.

Transonic flow around the NACA 0012 airfoil: For computation of inviscid flow around an NACA 0012 airfoil with a freestream Mach number of $M_\infty = 0.8$ and an angle of attack $\alpha = 1.25°$ the grid shown in Figure 8 is too coarse to get an acceptable shock resolution, and consequently these results are not shown here. At a finer grid, with 80 256 cells, 12 104 faces and 40 848 vertices, of which 1320 are located at the airfoil, we get the solution shown in Figure 11. At the leading edge, entropy is generated and total pressure losses are incurred. This increase in entropy causes boundary-layer-like viscous losses visible in the Mach isolines plot, which are also present for instance in the first-order results in Figure 4.1a of [49]. This numerical 'boundary layer' turns out to correspond to the region in which the entropy has increased considerably. As a consequence, the shock is too weak and located too far forward (but the Rankine–Hugoniot conditions are satisfied). The deviation from the benchmark is quite similar to what is generally observed with more classic first-order Euler solvers. In order to get a closer approximation of the AGARD benchmark solution [50], higher-oder methods with better conservation of total pressure are indispensable. Another cause of inaccuracy is that the outer boundary is not far enough from the airfoil and that the outer boundary conditions are not non-reflecting. Nevertheless, this example shows that a staggered discretization on

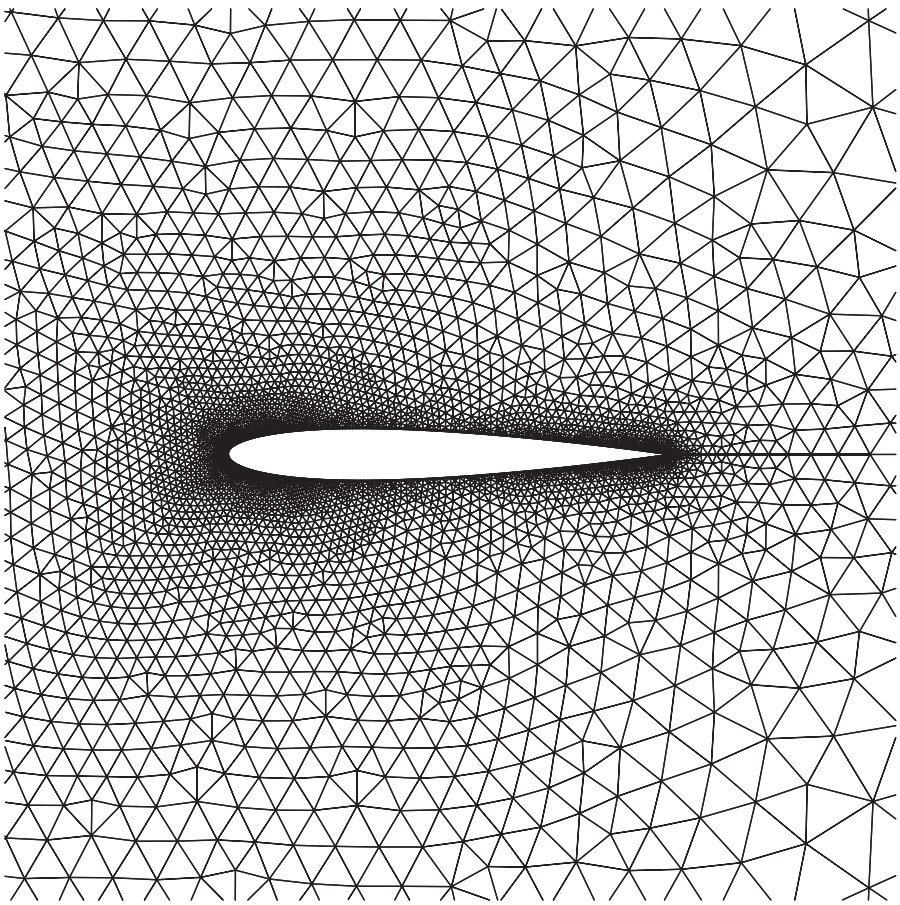

Figure 8. Part of the grid that is used to compute flows around the NACA 0012 airfoil.

unstructured grids can resolve transonic flows without causing spurious oscillations or other undesirable phenomena.

Supersonic flow around the NACA 0012 airfoil: Also for the supersonic flow case, with $M_r = 1.2$ and $\alpha = 0°$, around the NACA 0012 airfoil, the grid shown in Figure 8 turns out to be too coarse to get a good resolution of the shocks. On a grid with 31 144 cells, 46 931 faces and 15 787 vertices, of which 320 are positioned at the airfoil, that is refined in the vicinity of the shocks, we get the results depicted in Figure 12. The Mach isolines are almost identical to the ones shown in the AGARD benchmark solution [50]. In addition, the pressure distribution at the airfoil can hardly be distinguished from the AGARD result. Furthermore, even the result obtained at the grid of Figure 8, with 5002 vertices, turns out to yield a very accurate pressure distribution at the airfoil. So, apparently the lack of shock resolution does not prevent one from having a good agreement on the flow properties at the airfoil. The location of the sonic point upstream of the x-axis (-0.43 in our results; -0.42 in the AGARD

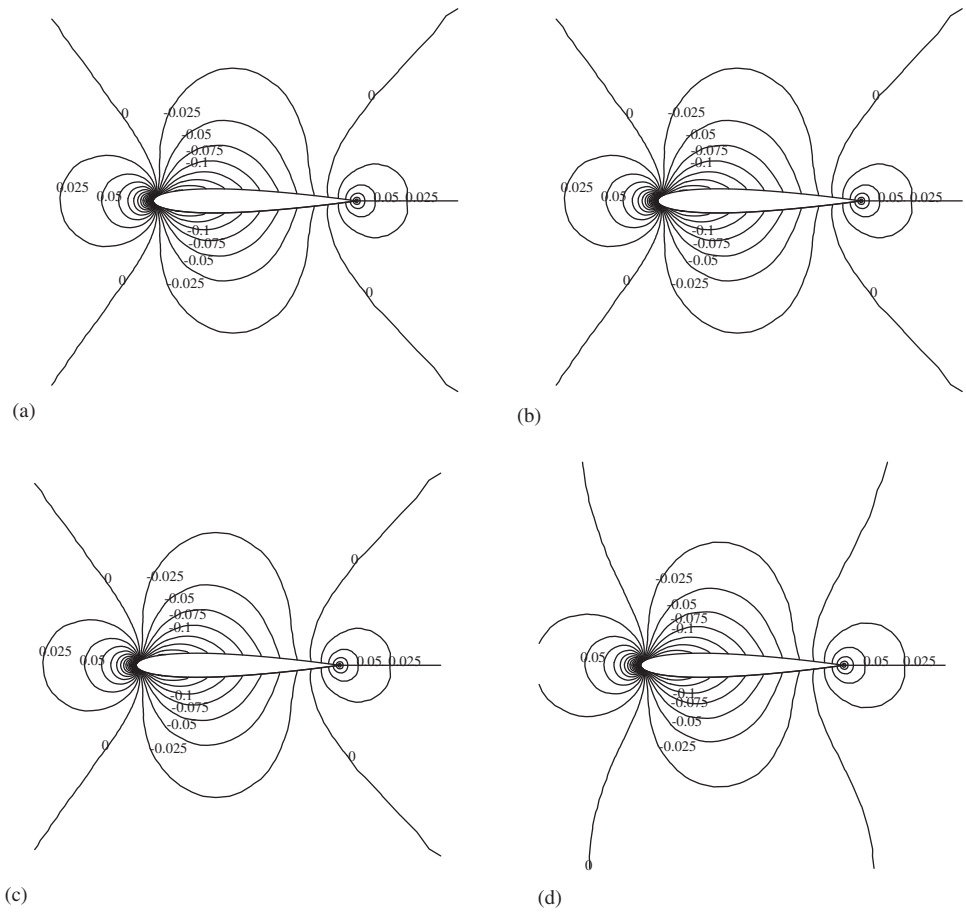

Figure 9. Isobars around NACA 0012 profile for $M_r = 0$ (a), $M_r = 10^{-3}$ (b), $M_r = 10^{-2}$ (c) and $M_r = 10^{-1}$ (d).

solution) and the value for the drag (0.0967 in our results; 0.0960 in the AGARD solution) are also in close correspondence with each other. This example shows that the unstructured staggered scheme is applicable to strongly compressible flows.

4.2.2. Mach uniform efficiency. In addition to the accuracy problem there is, for standard flow solvers, the problem of efficiency, i.e. the problem that computation time increases severely for low Mach number flows. In this section, we will show that the efficiency of the MU approach is uniform in the Mach number.

The computation time is mainly determined by the number of time steps needed to arrive at steady state and the amount of work per time step. Steady state is reached after N_t time steps at T_{end} ($T_{\text{end}} = N_t \Delta t$), where one time unit corresponds to the time needed to travel the distance of one chord length at freestream velocity. The relation between the Courant number

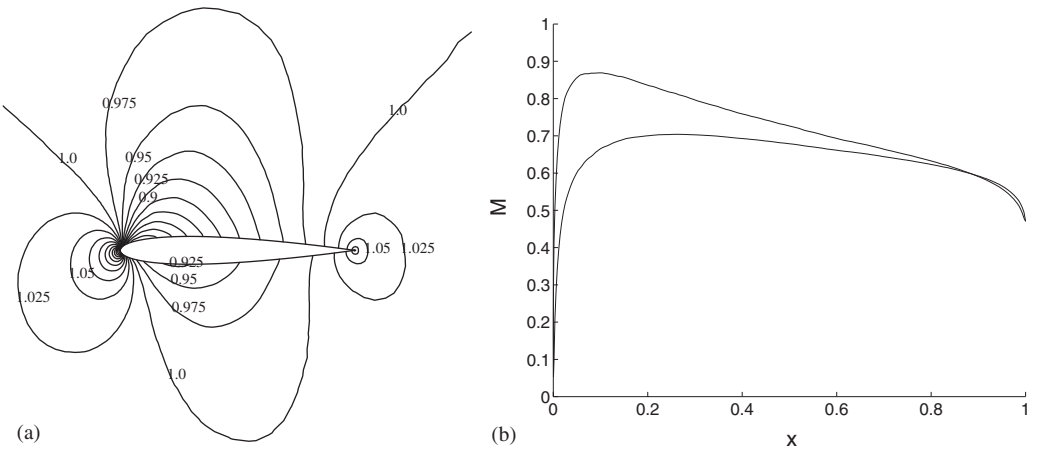

Figure 10. Subcritical flow around the NACA 0012 airfoil. Isobars (a) and Mach number at the airfoil (b).

and the time step is, up to a reasonable approximation, given by (in dimensionless units):

$$\sigma = \frac{(u_\infty + \sqrt{h_\infty}/M_\mathrm{r})\Delta t}{\Delta x} \tag{48}$$

where the particle velocity and the acoustic speed are based on the freestream values. The major part of work within a time step is devoted to the construction of linear systems, three in each time step, and solving them. The total number of solver iterations in the process of time stepping from initial to steady state is indicated by N_s, hence the average number of solver iterations per time step equals $n_s = N_s/N_t$. In Table I results for these various quantities are gathered as obtained during the computations described in Section 4.2.1, on the grid depicted in Figure 8. The time steps in this table are 'optimal', i.e. chosen such that the total computation time T_CPU is minimal; this is determined by means of trial and error. It turns out that then also N_s and N_t are minimal. If the time step is chosen slightly larger than this optimal time step, the transient behaviour becomes too strong, and numerical breakdown occurs; hence the optimal time step corresponds to the largest possible time step for which convergence is attained. As can be derived from the table, the fact that in the MU approach the pressure is taken implicitly allows for large Courant numbers. It is remarkable that, if the Courant number were defined as follows:

$$\tilde{\sigma} = \frac{u_\infty \Delta t}{\Delta x} \tag{49}$$

then the largest allowable value for $\tilde{\sigma}$ remains almost constant (between 80 and 90) over the whole range of Mach numbers $M_\mathrm{r} > 0$. The omission of the term $\sqrt{h_\infty}/M_\mathrm{r}$ can be made plausible by noting that the pressure, and hence the acoustic waves, are taken into account in an implicit manner.

By n_ρ, n_m and n_p we indicate the number of iterations in the linear solver to solve, respectively, the continuity, momentum and pressure-correction equation. Recall that one iteration in Bi-CGSTAB, which is used to solve the pressure-correction equation, is more expensive than

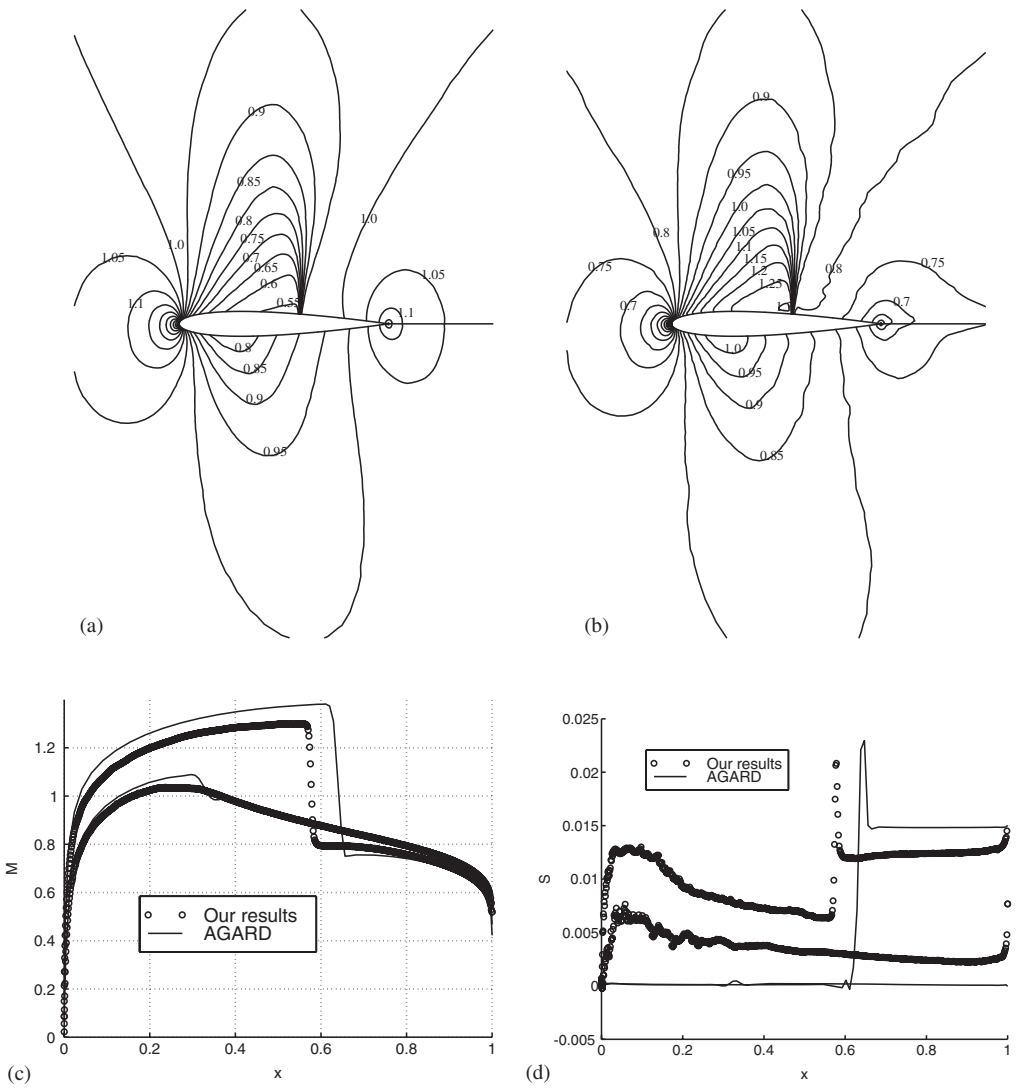

Figure 11. Transonic flow around the NACA 0012 airfoil computed on a fine grid. Isobars (a), Mach isolines (b), Mach number (c) and entropy (d) at the airfoil.

one GMRES iteration, which is utilized to solve the density and momentum equation. The reason why $n_s = N_s/N_t$ does not exactly satisfy $n_s = n_\rho + n_m + n_p$, is that the values for n_ρ, n_m and n_p are taken in the final steps of the time-marching procedure, where these values are constant and do not show the large variations that are present in the initial stage. The values for n_p, n_ρ and n_m are seen to increase for larger values of the time step, which is attributed to the $1/\Delta t$ behaviour of the main diagonal. This is demonstrated by additional experiments, whose results are not included in Table I. In addition, for a given time step, n_p is seen to decrease with increasing M_r, and this is caused by the M_r^2 term in the main diagonal.

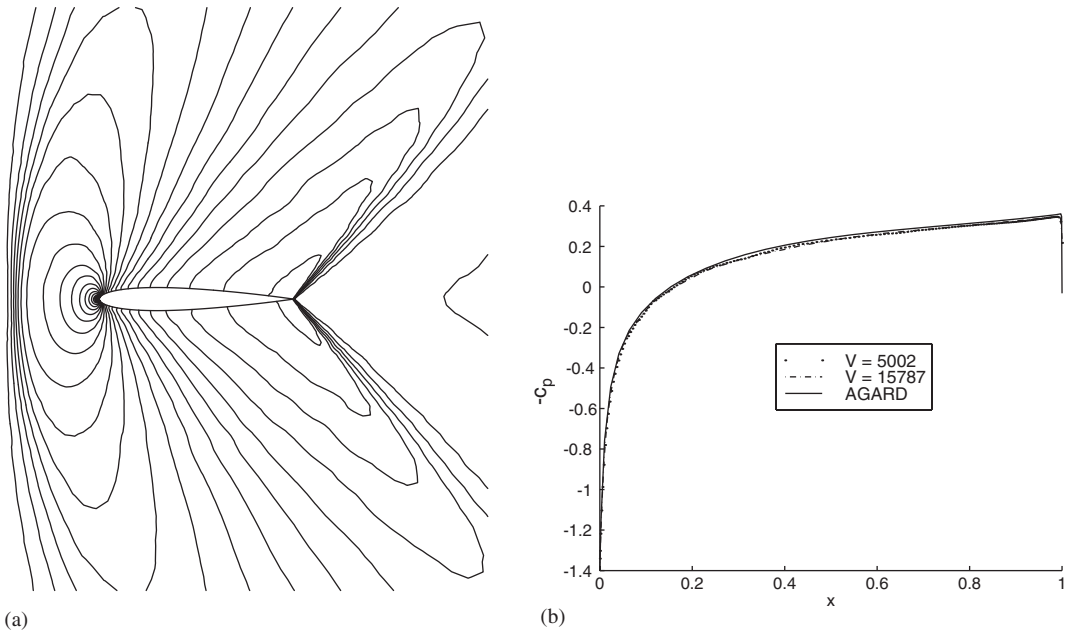

Figure 12. Supersonic flow around the NACA 0012 airfoil computed on a fine grid. Mach isolines (a) and pressure coefficient (b) at the airfoil.

Table I. Results related to efficiency of the airfoil computations.

M_r	0	0.1	0.63	0.8	1.2
Δt (10^{-2})	8.0	8.0	9.0	8.0	8.2
σ	—	800	233	180	150
T_{end}	4.72	2.96	17.2	49.5	52.5
N_t	59	37	191	619	642
T_{CPU} (s)	279	165	668	2021	1645
t_{CPU} (s)	4.73	4.46	3.50	3.26	2.56
N_s	6431	3853	14554	40828	30834
n_s	109	104	76.2	70.0	48.0
n_ρ	3	10	12	10	4
n_m	18	19	22	22	15
n_p	83	75	48	33	22

Clearly, Table I shows that T_{CPU} does not blow up as $M_r \downarrow 0$. This is the distinguishing feature of our method, as compared to methods based on extension of fully compressible methods to the weakly compressible case. In the fully compressible case the flow takes longer to settle down to steady state, necessitating more time steps; this effect would be irrelevant for instationary flows. The computing time per time step $t_{\text{CPU}} = T_{\text{CPU}}/N_t$ depends only weakly on M_r. We may say that the efficiency is uniform in the Mach number.

5. CONCLUSIONS

A Mach-uniform finite volume scheme on unstructured staggered grids for the 2D Euler equations has been presented. The Mach-uniform formulation is a generalization of the pressure-correction approach for incompressible flows, and is uniformly valid for Mach numbers ranging from 0 up to >1. The approach is pressure based, the variables are updated sequentially, and the scheme reverts back to the standard pressure-correction scheme for $M_r = 0$. Time integration is done with the implicit Euler method, and the resulting linear systems are solved by means of preconditioned Krylov subspace methods.

The grid consists of triangles. The scalar variables are located at the centroids of the triangles, whereas the normal momentum components are stored at the face centres. The continuity and pressure-correction equation are integrated over each triangle. For the momentum equations the control volume consists of the union of the two triangles adjacent to the face under consideration. For the evaluation of the pressure gradient the path-integral method is adopted. First-order upwind and central approximations for the numerical fluxes are presented, that require fewer operations than the numerical fluxes commonly used in colocated schemes.

Numerical results of subsonic flow in a channel with bump confirm that the current scheme is first-order accurate in space. Flows with different freestream Mach number, ranging from $M_r = 0$ up to $M_r = 1.2$, around the NACA 0012 airfoil are used to study the accuracy and efficiency of our schemes for incompressible and compressible flows. The accuracy does not degrade in the incompressible limit, and remains good even for supersonic flows. It is found that the Mach-uniform formulation is efficient over the whole range of Mach numbers. This is due to the fact that the pressure is taken implicitly, which enables the use of much larger time steps resulting in fewer time steps before convergence is reached. Quick convergence is obtained for Courant numbers typically in the order of a few hundred. The computing time does not blow up as $M_r \downarrow 0$, and the computing time per time step (for a given Δt) depends only weakly on M_r. We may say that the method is Mach-uniform in accuracy and efficiency.

ACKNOWLEDGEMENTS

I. Wenneker was supported by The Netherlands Organization for Scientific Research (NWO).

REFERENCES

1. Darmofal DL. Towards a robust multigrid algorithm with Mach number and grid independent convergence. In *Computational Fluid Dynamics '98*, vol. 2, Papailiou KD, Tsahalis D, Périaux J, Knörzer D (eds). Wiley: Chichester, 1998; 90–95.
2. Guillard H, Viozat C. On the behavior of upwind schemes in the low Mach number limit. *Computers and Fluids* 1999; **28**:63–86.
3. Koren B. Improving Euler computations at low Mach numbers. *International Journal of Computational Fluid Dynamics* 1996; **6**:51–70.
4. Koren B, van Leer B. Analysis of preconditioning and multigrid for Euler flows with low-subsonic regions. *Advances in Computer Methods* 1995; **4**:127–144.
5. Turkel E. Preconditioning techniques in computational fluid dynamics. *Annual Review of Fluid Mechanics* 1999; **31**:385–416.
6. Turkel E, Fiterman A, van Leer B. Preconditioning and the limit to the incompressible flow equations. *Report* 93-42, ICASE, NASA Langley, 1993.
7. Turkel E, Radespiel R, Kroll H. Assessment of preconditioning methods for multidimensional aerodynamics. *Computers and Fluids* 1997; **26**:613–634.

8. Weiss JM, Smith WA. Preconditioning applied to variable and constant density flows. *AIAA Journal* 1995; **33**:2050–2057.
9. Demirdžić I, Lilek Z, Perić M. A collocated finite volume method for predicting flows at all speeds. *International Journal for Numerical Methods in Fluids* 1993; **16**:1029–1050.
10. Hirt CW, Amsden AA, Cook JL. An arbitrary Lagrangian–Eulerian computing method for all flow speeds. *Journal of Computational Physics* 1974; **14**:227–253.
11. Lien FS. A pressure-based unstructured grid method for all-speed flows. *International Journal for Numerical Methods in Fluids* 2000; **33**:355–374.
12. Moukalled F, Darwish M. A high-resolution pressure-based algorithm for fluid flow at all speeds. *Journal of Computational Physics* 2001; **168**:101–133.
13. Bijl H, Wesseling P. A unified method for computing incompressible and compressible flows in boundary-fitted coordinates. *Journal of Computational Physics* 1998: **141**:153–173.
14. Harlow FH, Amsden AA. Numerical calculation of almost incompressible flows. *Journal of Computational Physics* 1968; **3**:80–93.
15. Harlow FH, Amsden AA. A numerical fluid dynamics calculation method for all flow speeds. *Journal of Computational Physics* 1971; **8**:197–213.
16. Shyy W, Chen M-H, Sun C-S. Pressure-based multigrid algorithm for flow at all speeds. *AIAA Journal* 1992; **30**:2660–2669.
17. van der Heul DR, Vuik C, Wesseling P. A staggered scheme for hyperbolic conservation laws applied to unsteady sheet cavitation. *Computing and Visualization in Science* 1999; **2**:63–68.
18. van der Heul DR, Vuik C, Wesseling P. A conservative pressure correction method for compressible flow at all speeds. *International Journal for Numerical Methods in Fluids* 2002; **40**:521–529.
19. Wesseling P. *Principles of Computational Fluid Dynamics*. Springer: Heidelberg, 2001.
20. Rhie CM, Chow WL. Numerical study of the turbulent flow past an airfoil with trailing edge separation. *AIAA Journal* 1983; **21**:1525–1532.
21. Wesseling P, Segal A, Kassels CGM. Computing flows on general three-dimensional nonsmooth staggered grids. *Journal of Computational Physics* 1999; **149**:333–362.
22. Wesseling P, Segal A, Kassels CGM, Bijl H. Computing flows on general two-dimensional nonsmooth staggered grids. *Journal of Engineering Mathematics* 1998; **34**:21–44.
23. Harlow FH, Welch JE. Numerical calculation of time-dependent viscous incompressible flow of fluid with a free surface. *The Physics of Fluids* 1965: **8**:2182–2189.
24. Mavriplis DJ. Unstructured grid techniques. *Annual Review of Fluid Mechanics* 1997; **29**:473–514.
25. Venkatakrishnan V. Perspective on unstructured grid flow solvers. *AIAA Journal* 1996; **34**:533–547.
26. Hall CA, Cavendish JC, Frey WH. The dual variable method for solving fluid flow difference equations on Delaunay triangulations. *Computers and Fluids* 1991; **20**:145–164.
27. Hall CA, Porsching TA. A characteristic-like method for thermally expandable flow on unstructured triangular grids. *International Journal for Numerical Methods in Fluids* 1996; **22**:731–754.
28. Hall CA, Porsching TA, Hu P. Covolume-dual variable method for thermally expandable flow on unstructured triangular grids. *International Journal of Computational Fluid Dynamics* 1994; **2**:111–139.
29. Hall CA, Porsching TA, Mesina GL. On a network method for unsteady incompressible fluid flow on triangular grids. *International Journal for Numerical Methods in Fluids* 1992; **15**:1383–1406.
30. Nicolaides RA. The covolume approach to computing incompressible flows. In *Incompressible Computational Fluid Dynamics*, Gunzburger MD, Nicolaides RA (eds). Cambridge University Press: Cambridge, UK, 1993; 295–333.
31. Nicolaides RA, Porsching TA, Hall CA. Covolume methods in computational fluid dynamics. In *Computational Fluid Dynamics Review 1995*, Hafez M, Oshima K (eds). Wiley: Chichester, 1995; 279–299.
32. Perot JB. Conservation properties of unstructured staggered mesh schemes. *Journal of Computational Physics* 2000; **159**:58–89.
33. Despotis GK, Tsangaris S. Fractional step method for solution of incompressible Navier–Stokes equations on unstructured triangular meshes. *International Journal for Numerical Methods in Fluids* 1995; **20**:1273–1288.
34. Despotis GK, Tsangaris S. A fractional step method for unsteady incompressible flows on unstructured meshes. *International Journal of Computational Fluid Dynamics* 1997; **8**:11–29.
35. Rida S, McKenty F, Meng FL, Reggio M. A staggered control volume scheme for unstructured triangular grids. *International Journal for Numerical Methods in Fluids* 1997; **25**:697–717.
36. Thomadakis M, Leschziner M. A pressure-correction method for the solution of incompressible viscous flows on unstructured grids. *International Journal for Numerical Methods in Fluids* 1996; **22**:581–601.
37. Klainerman S, Majda A. Compressible and incompressible flows. *Communications in Pure and Applied Mathematics* 1982; **35**:629–651.
38. Klein R. Semi-implicit extension of a Godunov-type scheme based on low Mach number asymptotics 1: one-dimensional flow. *Journal of Computational Physics* 1995; **121**:213–237.
39. Wenneker I, Segal A, Wesseling P. Conservation properties of a new unstructured staggered scheme. *Computers and Fluids* 2003; **32**:139–147.

40. Liou M-S, Steffen CJ. A new flux splitting scheme. *Journal of Computational Physics* 1993; **107**:23–39.
41. Jameson A. Analysis and design of numerical schemes for gas dynamics, 1: Artificial diffusion, upwind biasing, limiters and their effect on accuracy and multigrid convergence. *International Journal of Computational Fluid Dynamics* 1995; **4**:171–218.
42. Jameson A. Analysis and design of numerical schemes for gas dynamics, 2: Artificial diffusion and discrete shock structure. *International Journal of Computational Fluid Dynamics* 1995; **5**:1–38.
43. van Beek P, van Nooyen RRP, Wesseling P. Accurate discretization on non-uniform curvilinear staggered grids. *Journal of Computational Physics* 1995; **117**:364–367.
44. Hafez M, South J, Murmann E. Artificial compressibility methods for numerical solution of transonic full potential equation. *AIAA Journal* 1979; **17**:838–844.
45. Shashkov M, Swartz B, Wendroff B. Local reconstruction of a vector field from its normal components on the faces of grid cells. *Journal of Computational Physics* 1998; **139**;406–409.
46. Osher S, Solomon F. Upwind difference schemes for hyperbolic systems of conservation laws. *Mathematics of Computation* 1982; **38**:339–374.
47. Volpe G. Performance of compressible flow codes at low Mach numbers. *AIAA Journal* 1993; **31**:49–56.
48. Dervieux A (ed.). *Numerical Simulation of Compressible Euler Flows*. Notes on Numerical Fluid Mechanics, vol. 26, 1989.
49. Barth TJ, Jespersen DC. The design and application of upwind schemes on unstructured meshes. *AIAA Paper* 89-0366, 1989.
50. Yoshihara H, Sacher P. Test cases for inviscid flow field methods. *AGARDograph No.* 211, AGARD, Neuilly-sur-Seine, France, 1985.

